Adaptive merging of large datasets of a 3D measuring endoscope in an industrial environment

Hinz, Lennart, Kästner, Markus, Reithmeier, Eduard

Lennart Hinz, Markus Kästner, Eduard Reithmeier, "Adaptive merging of large datasets of a 3D measuring endoscope in an industrial environment," Proc. SPIE 11352, Optics and Photonics for Advanced Dimensional Metrology, 113520G (1 April 2020); doi: 10.1117/12.2553939

SPIE.

Event: SPIE Photonics Europe, 2020, Online Only, France

Adaptive Merging of Large Datasets of a 3D Measuring Endoscope in a Industrial Environment

Lennart Hinz[a], Markus Kästner[a], and Eduard Reithmeier[a]

[a]Institute of Measurement and Automatic Control, Nienburger Str. 17, Hannover, Germany

ABSTRACT

A 3D measuring endoscope with a small measuring head and parallel arrangement of the fibers can be guided into forming plants and carry out precise measurements of geometries which are unreachable for most three-dimensional measuring systems. The data obtained can be used to quantify the wear of highly stressed structures and thus provide information for maintenance. Due to the compact sensor design and the required accuracy, optics with small working distance and a small measuring volume are used. In addition to in situ single measurements of highly stressed structures, over a hundred individual measurements are conceivable in order to convert large and complex geometries into point clouds. Besides the robust and accurate registration of all measurements, merging is one of the main causes of inaccurate measurement results. Conventional merging algorithms merge all points within a voxel into a single point. Due to the large overlap areas required for registration, points of diverse quality are averaged. In order to perform an improved adaptive merging, it is necessary to define metrics that robustly identify only the good points in the overlapping areas. On the one hand, the 2D camera sensor data can be used to estimate signal-based the quality of each point measured. Furthermore, the 3D features from the camera and projector calibration can evaluate the calibration of a triangulated point. Finally, the uniformity of the point cloud can also be used as a metric. Multiple measurements on features of a calibrated microcontour standard were used to determine which metrics provide the best possible merging.

Keywords: metrology, fringe projection, point cloud, masking, merging

1. INTRODUCTION

New types of production processes such as sheet-bulk metal forming require real-time capable metrological solutions to continuously monitor the forming process. In addition to the complete geometrical inspection of the formed parts, it is also necessary to monitor the wear on critical geometries of the forming tools involved. This should be done, on the one hand, to minimize the risk of an unexpected failure or, on the other hand, to collect data to create an better understanding of the process itself in order to adjust specific parameters.[1] The need for real-time, holistic measuring techniques as well as the limited accessibility during the running forming-process with small openings and partially covered geometries exclude the traditional, tactile measuring techniques from this application.[2,3] By using a fiber-optic endoscopic fringe projection system, a very compact and flexible measuring head can be realised by spatial separation of the camera and projection unit and the actual measuring scene.[4,5]

2. PROBLEM

The fringe projection profilometry, which is based on the principles of triangulation, requires an overlapping of the viewing cones of the camera and projector and is thus susceptible to shadowing. Furthermore the quality of the measurement depends on the optical properties of the specimen.[5] For example, specular reflective or partially transparent geometries can limit a possible application. Further problems are aliasing effects of the projected fringes due to curved surfaces or surfaces outside the depth of field.[6] In order to mask corresponding implausible or noise induced measuring points, metrics are required to describe the quality of each triangulated point.

Further author information: (Send correspondence to Lennart Hinz)
Lennart Hinz: E-mail: lennart.hinz@imr.uni-hannover.de, Telephone: +49 - 511 - 762 3235

Optics and Photonics for Advanced Dimensional Metrology, edited by Peter J. de Groot, Richard K. Leach, Pascal Picart
Proc. of SPIE Vol. 11352, 113520G · © 2020 SPIE · CCC code: 0277-786X/20/$21 · doi: 10.1117/12.2553939

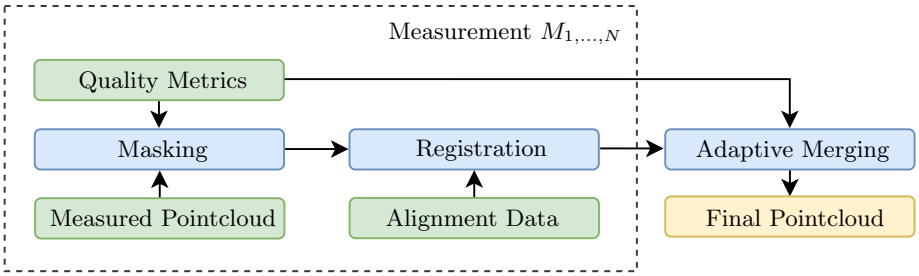

Figure 1: Basic procedure for stitching various individual measurements

Due to the imaging optics with small working distance and high magnification, very precise measurements can be performed in a small space. However, if larger areas are to be reconstructed, a combination with measurements from different poses is necessary.[5] This process, known as stitching, requires a combination of all measured point clouds in the overlapping areas to form a single point cloud. In conventional merging, redundant points are removed by combining all points within an imaginary volume element (usually a voxel) according to their center of gravity. This can lead to the merging of poorly measured points with well reconstructed points.[5] Adaptive merging, on the other hand, can select which points are retained and which are discarded by using appropriate metrics. Contrary to the classic cubic voxel, an imaginary sphere with radius d_s is used for each point, which ensures an even distance to all boundary surfaces of the volume element. d_s has to be chosen so that no grid average downsampling takes place, but at the same time points are merged at all. Therefore, the grid average distance d_{grid} of the reconstructed point cloud will be used as reference. d_{grid} is to be interpreted as a grid constant of the point cloud.

Figure 1 shows a simplified flowchart for stitching N single measurements. Operations like denoising or downsampling are neglected. The registration describes the exact alignment of the single measurements to each other. In order for the registration algorithms, such as the common iterative closest point (ICP) algorithm[7,8] to converge quickly and robustly, pre-alignment data is almost always necessary.[9,10] These can be derived, for example, from the position data of a kinematic robot in the case of a hand-eye calibration,[11] by matching corresponding, homologous features of a camera image pair[12] or by using computere aided design (CAD) data.[5] To perform the stitching as illustrated in figure 1, appropriate quality metrics must be identified and evaluated.

3. EXPERIMENTAL SETUP

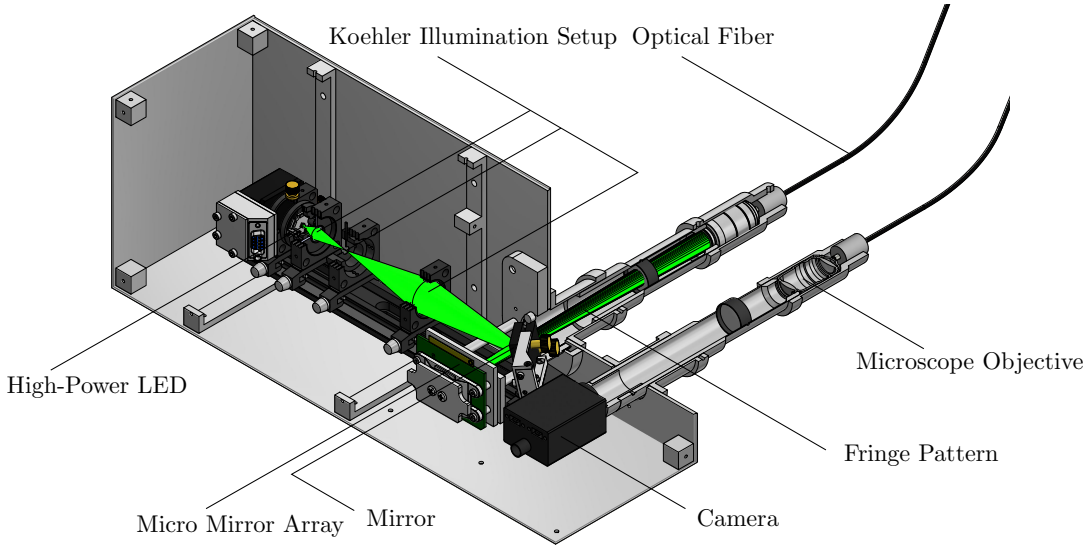

Figure 2: Overview of the camera and projection unit[5]

Figure 2 shows the setup and the main components of the measuring system used. From a high-power LED, supplied by OSRAM Licht AG (Munich, Germany), a homogeneous flat spot is imaged on a micro mirror array via a Koehler Illumination setup. The micro mirror array is supplied by Texas Instruments (Dallas, TX, USA). The fringe patterns created there by binary tilting of the individual mirrors are injected via a microscope lens into an optical fiber bundle (Fujikura Ltd., Tokio, Japan) with 100,000 individual fiber cores. The fringes are imaged onto the fiber bundle end in the measuring head. A triangulation base of 30 degree is formed in the measuring head and gradient index (GRIN) rod lenses with 10 mm working distance are used as imaging optics. They are supplied by Grintech GmbH (Jena, Germany). On the camera side, the scenery is imaged onto a CMOS camera of the type PointGrey US3-U3-23S6M-C (FLIR Integrated Imaging Solutions GmbH, Ludwigsburg, Germany) with an identical image fiber bundle and microscope lens.

As shown in figure 1, each individual measurement is first masked, then registered and finally an adaptive merging is performed. Position data of a linear stage are used for pre-alignment. The final result is examined with regard to deviation and the number of remaining points. To evaluate the effectiveness and suitability of the quality metrics appropriate features of geometric reference objects are reconstructed and the deviation is quantified. The introduction of those metrics, which can basically be divided into signal-based, calibration-based and geometry-based, is set out in section 4. For the signal intensity based approaches, planar reflection standards are used to investigate the suitability of the metrics under varying reflection conditions. Since a larger expansion within the measurement volume is preferable for the threshold value analysis with the calibration-based methods, a diffuse spherical standard which is supplied by Kolb & Baumann GmbH & Co. KG (Aschaffenburg, Germany), is used here. The geometric metric is also evaluated on this object. To describe the deviation, a two step fit (according to sphere, plane or cylinder equation) with 3 sigma inlier[13] performed using a least squares approach.[14]

As a final investigation, an adaptive merging based on the metrics and identified threshold values will be carried out. In this case, a cylindrical feature on a microcontour standard (Alicona Imaging GmbH, Graz, Austria), shown in figure 3, is reconstructed from two different measurement poses. Both individual measurements are to be masked first and then merged adaptively.

After fitting the combined point cloud, several characteristic values can be used to quantify the results:

- The deviation d_r of the fitted feature (radius) from the specification in the calibration certificate.
- The standard deviation σ_{dev} of all points to the fitted reference geometry.
- The remaining number of points.

Figure 3: Micro contour standard with reference cylinder

4. QUALITY METRICS

The metrics examined can be divided into three classes. The signal-based approaches aim to describe the quality of each triangulated point by means of different characteristics of the corresponding camera pixels. On the other hand, the idea is to identify and remove badly calibrated points by taking into account the local calibration quality, which is expressed in the form of calibration-based procedures. Lastly, a point cloud based approach is also considered as a quality metric, identifying bad points as non-uniform outliers in their local neighbourhood.

4.1 Signal based quality metrics

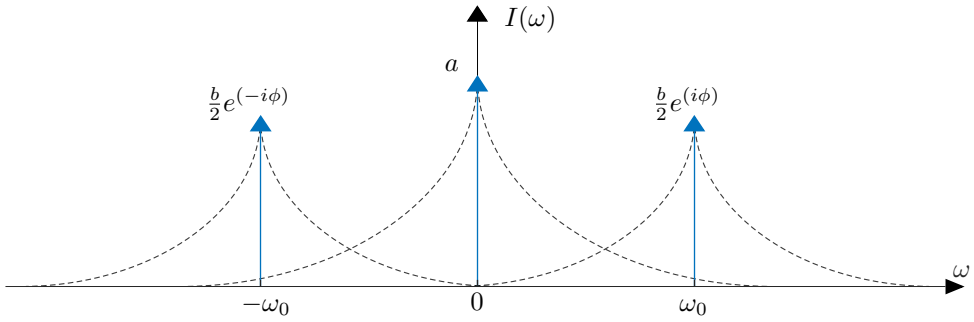

Figure 4: Exemplary spectrum of a temporal carrier phase-modulated fringe pattern

The projected fringe patterns to solve the correspondence problem uses the common phase-coded projection approach, in which sinusoidal patterns are projected onto the scene via a temporal phase-shifted projection sequence.[15–17] From the viewpoint of the camera, the idealized stationary fringe pattern for each pixel can typically be described according to equation 1.[18,19] Noise influences are neglected.

$$I(u_c, v_c, t) = a(u_c, v_c) + b(u_c, v_c)cos[\phi(u_c, v_c) + \omega_0 t] \tag{1}$$

Where u_c, v_c represent the camera pixel coordinates, $w_0 t$ corresponds to the temporal-carrier phase modulation, $\phi(u_c, v_c)$ represents the phase function for triangulation. $a(u_c, v_c)$ and $b(u_c, v_c)$ represent the background and the local contrast respectively the DC and the cosine component of the corresponding spectrum of the sinusoidal fringe pattern as shown in figure 4. Typical algorithms for phase retrieval, depending on the number of phase shift steps, are based on linear filters and are only mentioned here.[19–21] The figure shows for two projections on one plane how the individual components for a focused and an out-of-focus image are affected.

Figure 5a shows a single row from the camera image for a focused projection on a plane and the signal components contained in it. Figure 5b shows a row from a poorly focused image for comparison, which is examined analogously. It is assumed that the last image contains rather poor and noisy pixels and therefore many reconstructed points lead to a higher measurement uncertainty and deviation. It can be observed that the fringe amplitude decreases faster than the actual background intensity. In the following, three different metrics are described, which refer to the corresponding signal components.

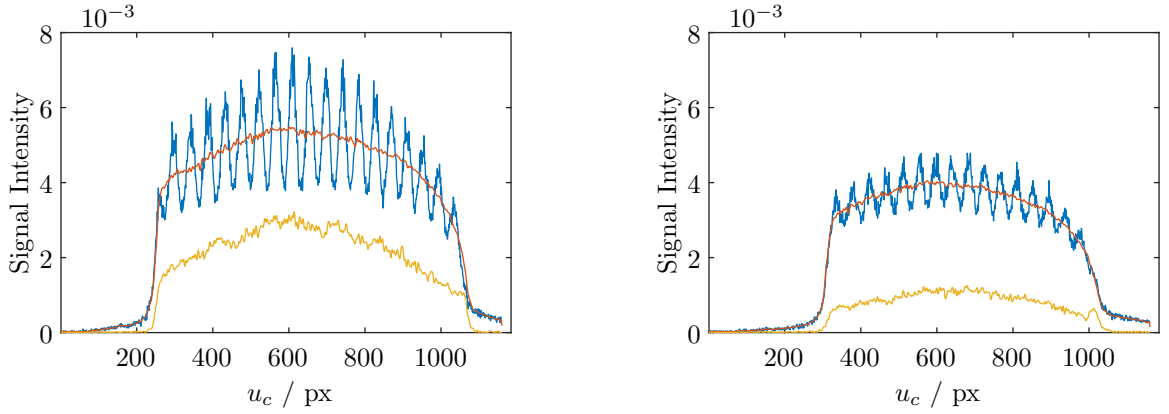

(a) In focus (b) Out of focus

Figure 5: Characteristics of the corresponding signal components for an image row for different focus positions when projected onto a plane (blue: $I(u_c, 1)$, orange: $a(u_c)$, yellow: $b(u_c)$)

Signal strength A basic filtering is first of all achieved by masking via the general signal strength $b(u_c, v_c)$ which corresponds to the fringe amplitude according to figure 5 and equation 1. The idea behind this is that bright pixels with correspondingly high gray scale values represent good illumination and are therefore considered plausible, while dark pixels are more likely to be noisy and can be excluded. The influence of background brightness is not taken into account.

Signal attenuation In this case the fringe amplitude is normalized pixel by pixel to $a(u_c, v_c)$. Since image sharpness in the frequency spectrum can be quantified by attenuations of higher orders to the DC component, a certain analogy to the sharpness of the image is given.[22] Local image sharpness is analogous to sharp and contrasty edges in the image which makes an application of classical, image processing local operators (like Laplacian or Sobel-Kernels[23]) also conceivable. But in this case spectral properties were decidedly preferred to spatial ones.

Phase shift variation The last concept examines the masking by the pixelwise local standard deviation of the observed projection σ_I. Since there may be additional projections with varying frequency in the projection sequence for unambiguous phase-unwrapping, in this case the camera images at the highest fringe frequency are used. The procedure follows the approach to assume that a proper triangulation is proportional to a significant variation of the respective pixel over the projection sequence.

4.2 Calibration based quality metrics

A signal-based quality metric can make a possible statement about how reliable a pixel is acquired and how plausible the corresponding triangulated three-dimensional object point is. No statement can be made about the quality of the reconstructed point in relation to the applied calibration and the associated model deviations.

A stereoscopic triangulation system requires an appropriate calibration of the imaging planes involved. In this case the camera and the projector are calibrated according to the widely used pinhole camera model[24] by optimizing the unknown calibration parameters K and T from equation 2.[25–27]

$$w \begin{bmatrix} I_P \\ 1 \end{bmatrix} = KT \begin{bmatrix} P \\ 1 \end{bmatrix} \tag{2}$$

According to figure 6, P refers to a three-dimensional object point, I_P is the intersection of the corresponding view beam to the camera center with the pixel sensor. T is the rigid body transformation from the pixel sensor's coordinate system $(KS)_I$ to the camera center $(KS)_C$, which is also called extrinsic calibration. K is called intrinsic calibration and describes the position of the image principal point and the focal lengths within the pinhole camera model. In order to approximate the required parameters, an appropriate calibration procedure is used, which is based on the positioning of a defined calibration standard and appropriate markers within the measuring volume. To take the imaging properties of the optics into account, radial and tangential distortion is additionally calibrated and corrected before each triangulation.[28]

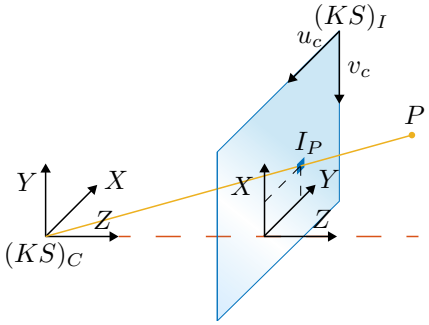

Figure 6: Pinhole camera model

The typical metric to describe the model deviation for each calibrated feature is the reprojection error.[27] Figure 7 shows the norm of the reprojection error for the camera and projector relative to each feature location after calibration. On the basis of this representation, basically three approaches can be introduced, which can be used as a metric for each triangulated point. Another special feature of the calibration-based masking metrics is that a quality metric can be calculated for the calibrated camera and projector features.

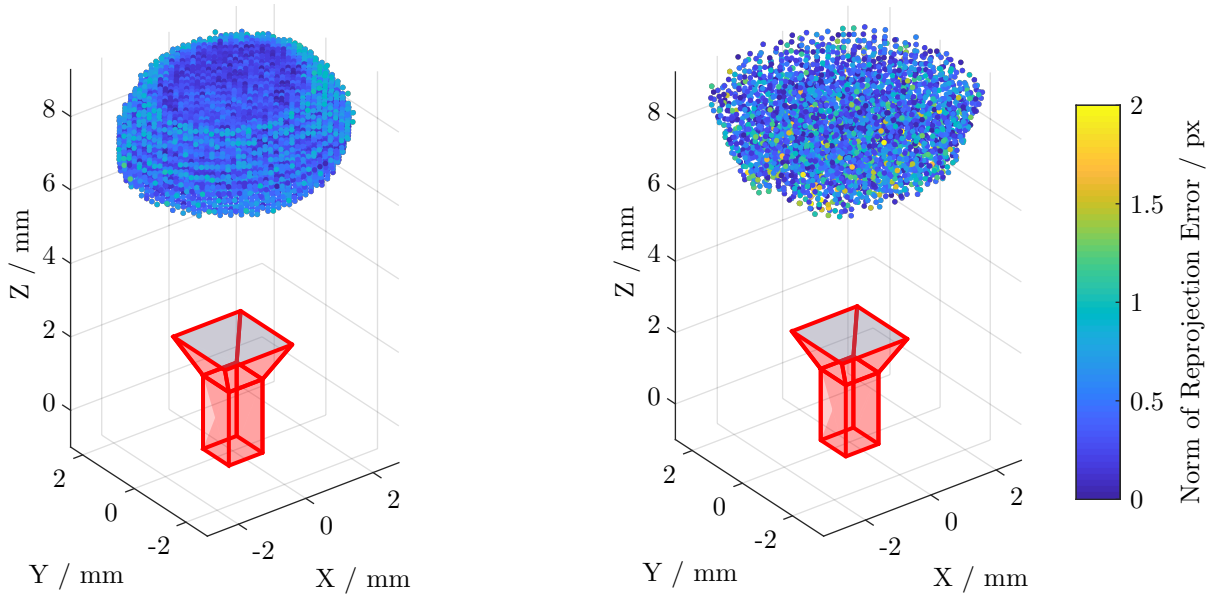

(a) Camera (b) Projector

Figure 7: Location of all calibrated features, colored according to the norm of the reprojection error in the corresponding pixel coordinate system

Reprojection error of the nearest calibrated feature In this case, no additional metric needs to be introduced in order to evaluate the local calibration quality. The reprojection error of the feature closest to each point of the triangulated point cloud is therefore applied. For this purpose, a one nearest neighbor (1-NN) classification is performed between the triangulated point cloud and the point cloud of the calibrated features using the fast KD tree.[29,30] The Euklidean norm of each reprojection error $rep_{err}(f_i)$ for each corresponding feature f_i serves as a threshold for further masking.

Local feature density of the nearest calibrated feature A density-based metric is introduced to address the possibility that certain regions in the measurement volume may not have been sufficiently considered in the process of modeling due to a small number of features. First, the local density of the feature point cloud is determined and then re-classified to 1-NN to assign the density of the feature point cloud to the actual measured point cloud for each feature and triangulated point. The local density ρ_i for each point p_i is calculated as shown in equation 3.[31]

$$\rho_i = \sum_j (d_{ij} < d_c) \tag{3}$$

Where d_{ij} is the Euclidean distance of each point p_j to point p_i and d_c is the cut-off distance, which is chosen so that the average number of neighbours is about 1-2 percent of the total number of points.[31]

Distance to the nearest calibrated feature A different approach to the possibly inadequate local weighting during calibration according to the pinhole camera model is given by the Euclidean distance $d_{cal,NN}$ to the nearest calibrated feature. The graphical representation of the metric for each point of the reconstructed point cloud is shown in figure 8.

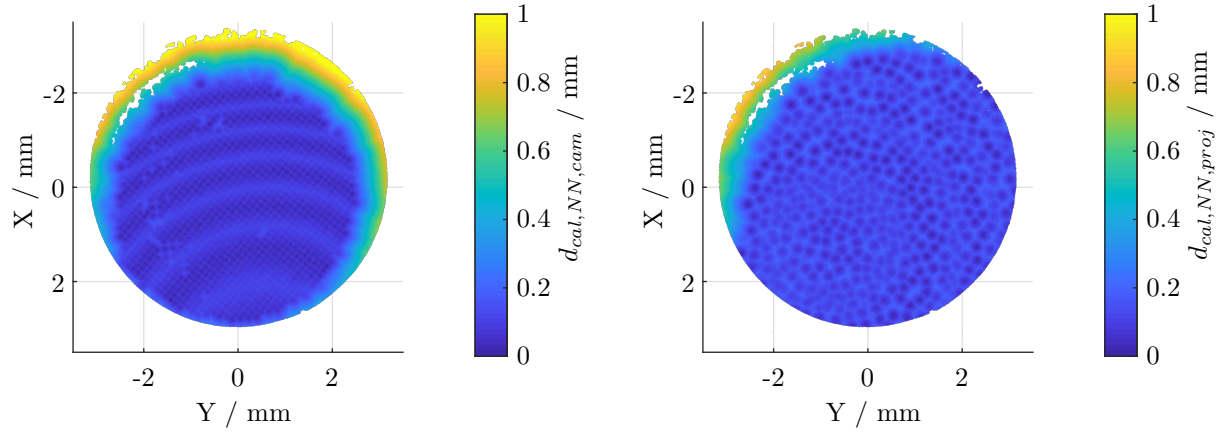

(a) Distance of the point cloud to the nearest calibrated camera feature

(b) Distance of the point cloud to the nearest calibrated projector feature

Figure 8: Comparison of calibration-based quality metrics according to camera and projector representation based on the distance to the nearest calibrated feature

4.3 Point cloud based quality metric

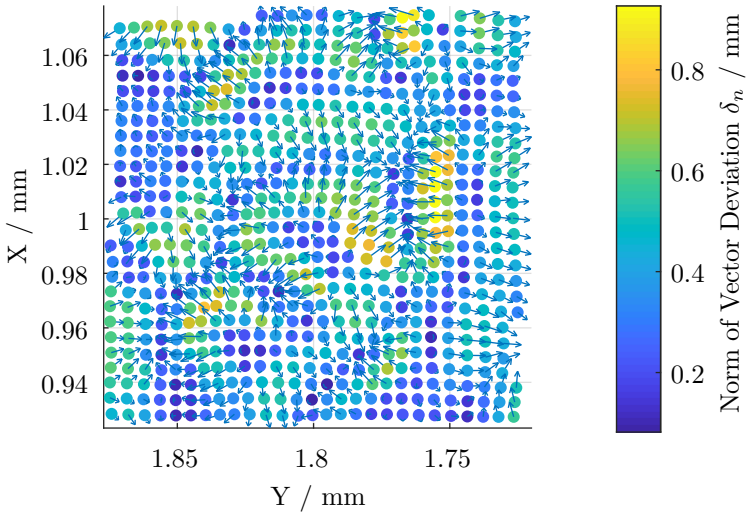

Figure 9: Local non-uniformity of the point cloud characterized by the application of the metric δ_n

An alternative approach for a possible quality metric is given by the local uniformity of a point cloud. One way to describe this is the deviation of the normal vector n_i of each point p_i from the mean normal. For the determination of the normal a plane fitting with neighboring points is performed.[32] The range in which the mean normal vector is determined is to be selected accordingly much larger. The deviation can then be calculated using the Euklidean norm of the difference of both vectors according to equation 4. Where N is the number

of neighboring points p_j used to determine the mean normal and varies between 61 and 241 at a fixed radius (*rangeserach*) of 50 μm. An angle-based approach is also conceivable.

$$\delta_{n,i} = \|n_i - \frac{1}{N}\sum_{j=1}^{N} n_j\|_2 \tag{4}$$

Figure 9 shows the use of this metric on a very small part of the measurement data. Local variations in the point cloud, which can be described by the metric, are clearly visible.

5. RESULTS - MASKING

5.1 Signal based quality metrics

Measurements on the diffuse plane standard Figure 10 shows the threshold characteristics of the signal intensity based metrics on a diffuse reflectance standard. The influence on the standard deviation of all deviations σ_{dev} and the remaining number of points is examined. It can be observed that there is a level of deviation of about $\sigma_{dev} \sim 5$ μm, which in principle can be robustly masked by all approaches. It is therefore concluded that the higher deviations are due to effects that all metrics can quantify. The variable exposure time also has a certain influence on the threshold response. Overall, the approach according to the standard deviation over the phase shift sequence shows the best results, since the implausible points can be discarded very robustly and quickly, the exposure time hardly shows any influence and a threshold value determination with which as many points as possible are retained is feasible.

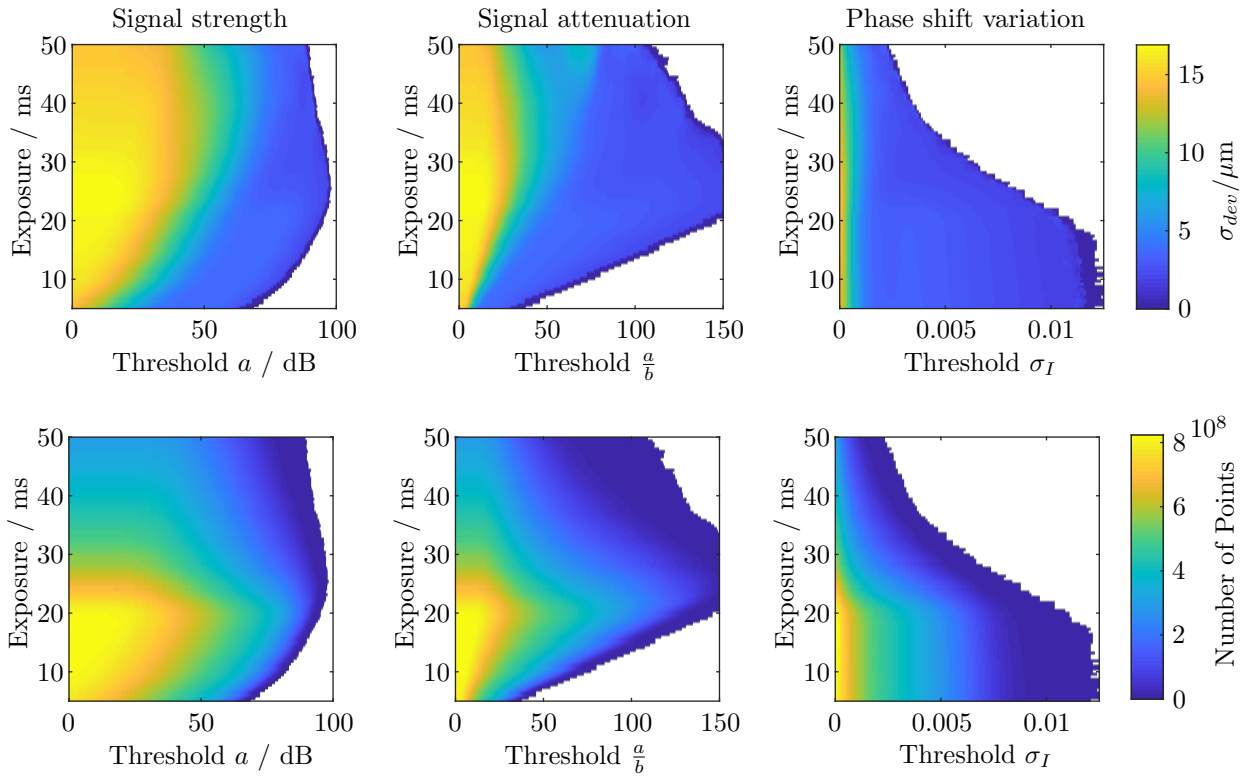

Figure 10: Influence of masking according to the different signal-based metrics on the standard deviation of all deviations σ_{dev} and the remaining number of points

Measurements on other technical surfaces To also investigate less optimal technical surfaces, experiments were also carried out on planar samples with different optical properties. For this purpose high dynamic range (HDR) sequences were captured. This ensures that even specular surfaces can be imaged and possibly reconstructed. The results are shown in figure 11. As before, masking via σ_I shows the best results, since a threshold value is possible for all surfaces and the deviation is thus relatively evenly reduced to a lower level. The other approaches seem susceptible to bright spots, do not allow for a uniform threshold value and show inconsistent behavior for different surfaces.

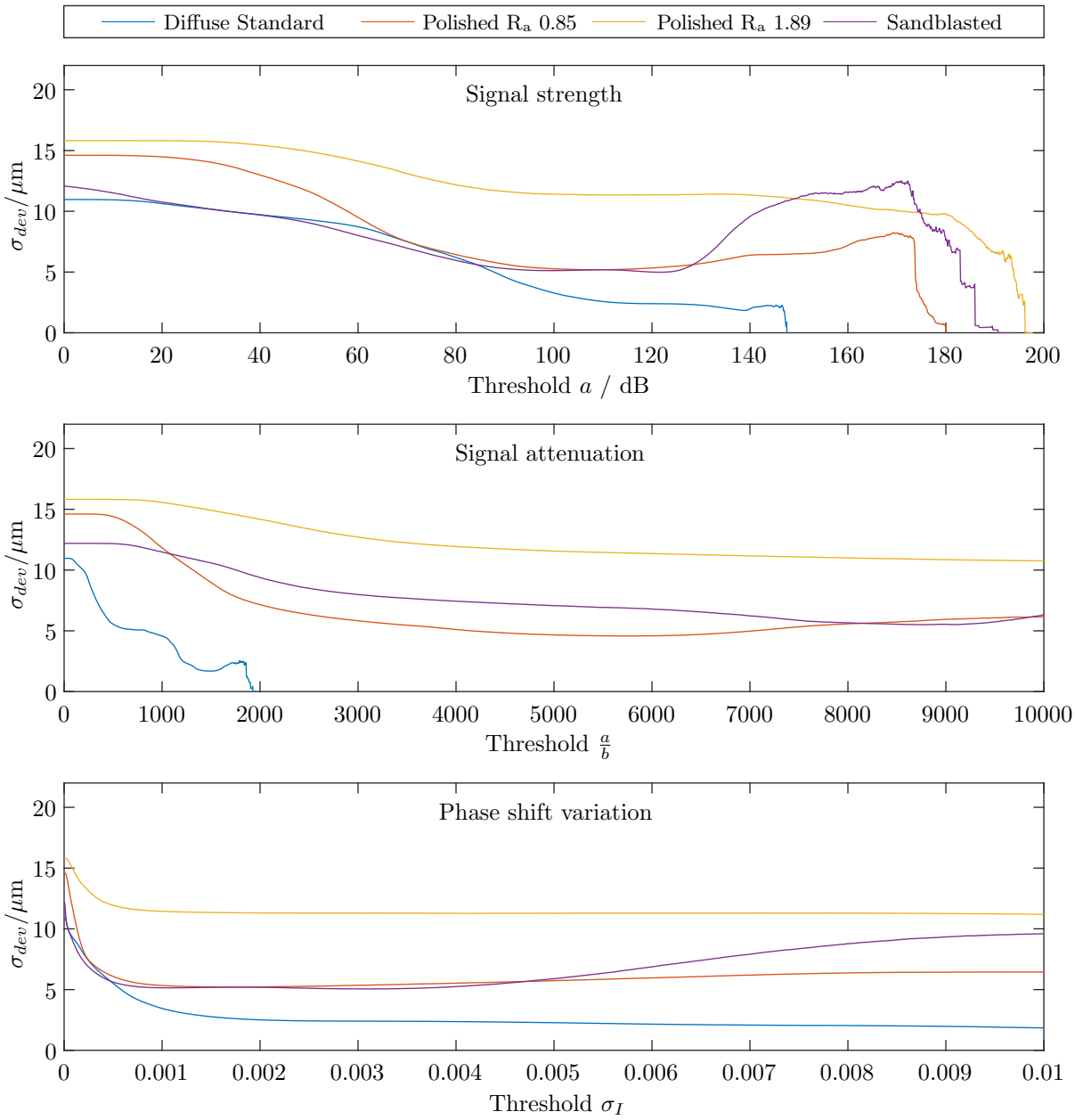

Figure 11: Comparison of the threshold behavior of different signal-based masking metrics for different technical surfaces

5.2 Calibration based quality metrics

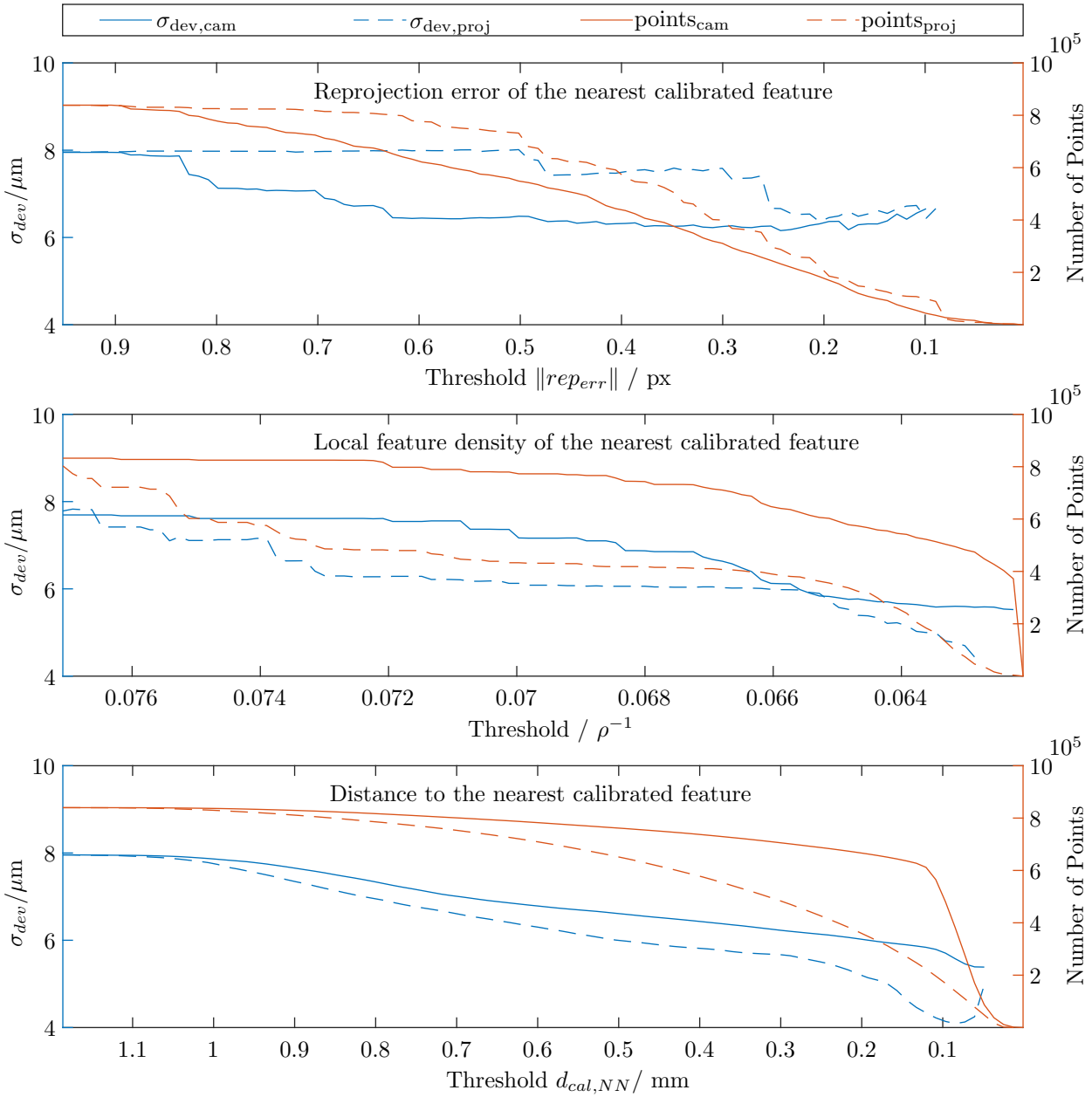

Figure 12: Comparison of the threshold behavior of different calibration-based masking metrics using the calibrated camera or projector features

Figure 12 shows the response of the point cloud deviation and the number of remaining points as depending on the different calibration based quality metrics. In principle, all approaches provide better results, but it can be observed that taking into account the reprojection error of the nearest feature cannot mask the point cloud in such a way that the lowest level of deviation is obtained. The best results are provided by the Euclidean distance to the next calibrated feature. It can be seen that the use of the camera features up to a threshold of about 0.1 mm reduced the deviation from about 8 to 6 μm, but only a few points were removed. The point density approach shows a similar behaviour, but masks more points for a comparable deviation level and is a bit more discontinuous by setting the density of the next calibrated feature.

5.3 Point cloud based quality metric

Figure 13 shows the response to the reciprocal of the geometric threshold δ_n^{-1}, which expresses how much the normal vector of each reconstructed point differs from the mean normal within the neighbourhood. Thus, the threshold allows uneven points to be discarded, as confirmed by the characteristics in Figure 13. However, it also shows that the number of remaining points decreases very quickly and a reduction of the deviations is only possible with great restrictions.

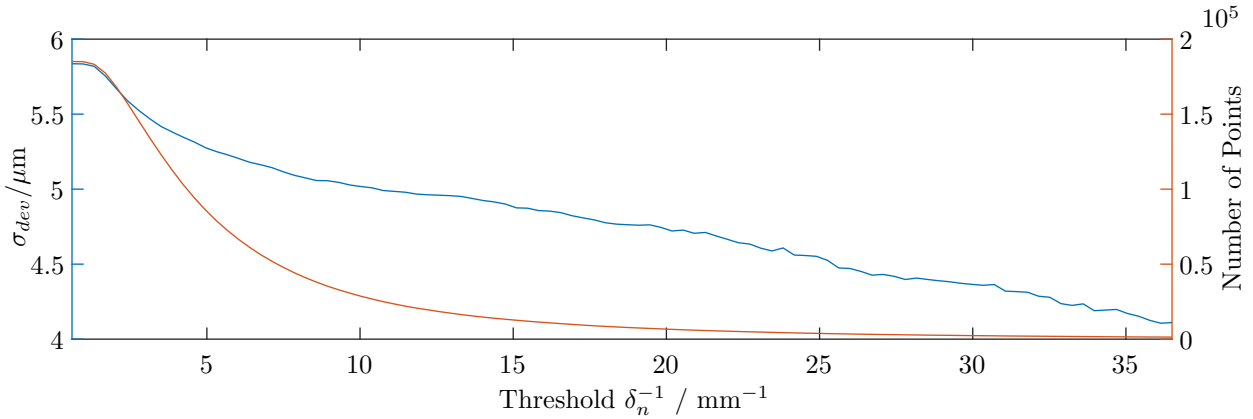

Figure 13: Influence of the point cloud based threshold δ_n^{-1} on the deviation and the number of points

6. RESULTS - ADAPTIVE MERGING

In accordance with the observations made previously (section 5), two individual measurements from different measuring positions are now to be merged into a single point cloud as described in figure 1. It has been observed that the masking via the variation of the phase shift σ_I of the highest frequency and the masking via the distance $d_{cal,NN,cam}$ of the reconstructed point cloud to the nearest calibrated feature show good results in terms of reducing the deviations and maintaining as many points as possible. The latter metric is simplified as d_{cal} in the following. A cylindrical feature on the micro contour normal from figure 3 serves as the measurement object. According to section 5, d_{cal} is set at 150 μm and σ_I at 0.002. The results are shown in figure 14, with each diagram representing one of the assessment dimensions introduced in section 3. The possible masking metrics already examined are vertically listed, whereby the combination of the two approaches is also examined. The possible quality metrics for adaptive spherical merging are listed horizontally, with the point cloud-based approach with the threshold δ_n^{-1} also being examined. The measured cylinder has a radius of 1001.5±0.7 μm according to the calibration certificate.

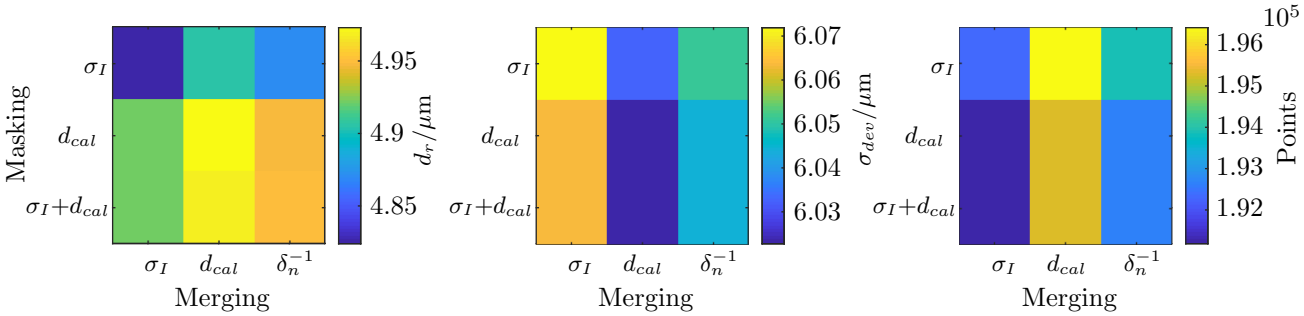

Figure 14: Effect of different masking and merging metrics on the final result of the combined measurement ($d_r \sim d_{grid}$)

The results are inconclusive. In general, the combination of both masks does not provide a demonstrable advantage. However, this may also be due to the fact that the measured object is located in the closely calibrated area in

front of the sensor. Therefore, it cannot be excluded that the combination is advantageous at another position in the measuring volume. Merging by σ_I seems to minimize the deviation of the fitted feature from the reference d_r, but at the same time produces the point cloud with the highest variation σ_{dev} and the lowest number of points.

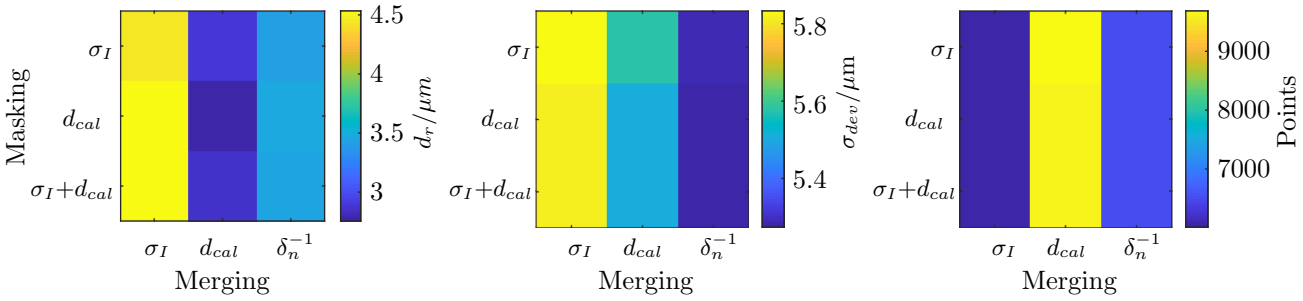

Figure 15: Effect of different masking and merging metrics on the final result of the combined measurement ($d_s \sim 5\ d_{grid}$)

To increase the effect of the merging on the results, the radius of the sphere d_s is increased to $\sim 5\ d_{grid}$. As described in section 2, this is analogous to a grid average downsampling, as the number of total points is strongly reduced. The results are shown in figure 15. It turns out that merging according to σ_I provides the poorest results in terms of d_r and σ_{dev} and the number of points. It is remarkable that the merging according to δ_n^{-1} results in the most even point cloud. Merging according to d_{cal} shows the best results regarding the number of points and d_r. It also has a relatively even point cloud according to σ_{dev}.

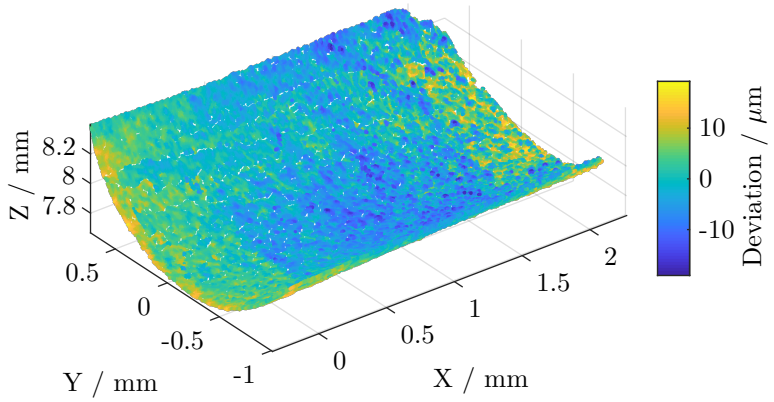

Figure 16: Final point cloud after merging using d_{cal} ($d_s \sim 2\ d_{grid}$)

7. CONCLUSION

The choice of appropriate metrics for point cloud masking has been shown to have a significant impact on the accuracy of the reconstruction. Taking into account the number of remaining points, signal intensity based masking via the standard deviation of the phase shift sequence and calibration based masking via the distance to the next calibrated camera feature provides the best results. Since the specific influence depends on the positioning in the measurement volume or the reflection properties of the specimen, a combination of both approaches seems to be reasonable, although no advantage could be demonstrated in section 6. The following merging only has a significant influence if the size of the neighboring sphere is increased in such a way that a grid average downsampling takes place at the same time. This may also be due to the fact that the local noise is larger than the actual grid distance within the point cloud and points may not be combined although theoretically they

belong together. Comparable results as in figure 15 could also be achieved with significantly smaller spherical radii. In this case, the merging using the calibration-based metric shows good results, whereas the signal-based approach performs worst. A point cloud of the reconstructed cylinder feature masked and combined in this way is finally shown in figure 16.

ACKNOWLEDGMENTS

The authors would like to thank the German Research Foundation (DFG) for funding the project B6 "Endoscopic geometry inspection" within the Collaborative Research Center (CRC) / TR 73.

REFERENCES

[1] Kleiner, M., Geiger, M., and Klaus, A., "Manufacturing of lightweight components by metal forming," *CIRP Annals - Manufacturing Technology* **52**, 521–542 (12 2003).

[2] Frankowski, G. and Hainich, R., "Dlp-based 3d metrology by structured light or projected fringe technology for life sciences and industrial metrology," *Proceedings of SPIE - The International Society for Optical Engineering* **7210** (02 2009).

[3] Weckenmann, A., Krämer, P., and Hoffmann, J., "Manufacturing metrology - state of the art and prospects," 1–8 (01 2007).

[4] Matthias, S., Loderer, A., Koch, S., Gröne, M., Kästner, M., Hübner, S., Krimm, R., Reithmeier, E., Hausotte, T., and Behrens, B.-A., "Metrological solutions for an adapted inspection of parts and tools of a sheet-bulk metal forming process," *Production Engineering* **10** (12 2015).

[5] Hinz, L., Kästner, M., and Reithmeier, E., "Metal forming tool monitoring based on a 3d measuring endoscope using cad assisted registration," *Sensors* **19**, 2084 (05 2019).

[6] Peng, T. and Gupta, S., "Algorithms for generating adaptive projection patterns for 3d shape measurement," *Journal of Computing and Information Science in Engineering - JCISE* **8** (01 2008).

[7] Horn, B., "Closed-form solution of absolute orientation using unit quaternions," *Journal of the Optical Society A* **4**, 629–642 (04 1987).

[8] Besl, P. and McKay, N., "A method for registration of 3-d shapes," *IEEE Trans. Pattern Anal. Mach. Intell.* **14**, 239–256 (04 1992).

[9] Recherche, E., Automatique, E., Antipolis, S., and Zhang, Z., "Iterative point matching for registration of free-form curves," *Int. J. Comput. Vision* **13** (07 1992).

[10] Faugeras, O. and Hebert, M., "The representation, recognition, and locating of 3-d objects," *International Journal of Robotic Research - IJRR* **5**, 27–52 (09 1986).

[11] Horaud, R. and Dornaika, F., "Hand-eye calibration," *I. J. Robotic Res.* **14**, 195–210 (06 1995).

[12] Lin, C.-C., Tai, Y.-C., Lee, J.-J., and Chen, Y.-S., "A novel point cloud registration using 2d image features," *EURASIP Journal on Advances in Signal Processing* **2017** (12 2017).

[13] Verein Deutscher Ingenieure (VDI), "VDI/VDE 2634: Optical 3-D measuring systems - Optical systems based on area scanning," (2012).

[14] Eberly, D., "Least squares fitting of data," *Chapel Hill, NC: Magic Software* (01 2000).

[15] Servín, M., Estrada, J., and Quiroga, J., "The general theory of phase shifting algorithms," *Optics express* **17**, 21867–81 (11 2009).

[16] Salvi, J., Pages, J., and Batlle, J., "Pattern codification strategies in structure light systems," *Pattern Recognition* **37**, 827–849 (04 2004).

[17] Gorthi, S. S. and Rastogi, P., "Fringe projection techniques: Whither we are?," *Optics and Lasers in Engineering* **48** (02 2010).

[18] Surrel, Y., "Design of algorithms for phase measurement," (09 1998).

[19] Servín, M., Quiroga, J., and Padilla, M., "Fringe pattern analysis for optical metrology: Theory, algorithms, and applications," *Fringe Pattern Analysis for Optical Metrology: Theory, Algorithms, and Applications* , 1–327 (01 2014).

[20] Freischlad, K. and Koliopoulos, C., "Fourier description of digital phase-measuring interferometry," *Journal of The Optical Society of America A-optics Image Science and Vision - J OPT SOC AM A-OPT IMAGE SCI* **7** (04 1990).

[21] Creath, K., "V phase-measurement interferometry techniques," *Progress in Optics* **26** (12 1988).

[22] Vu, C. and Chandler, D., "S(3): A spectral and spatial sharpness measure," *Proceedings - 2009 1st International Conference on Advances in Multimedia, MMEDIA 2009* , 37–43 (07 2009).

[23] Krotkov, E. and Martin, J.-P., "Range from focus," 1093 – 1098 (05 1986).

[24] Hartley, R. and Zisserman, A., [*Multi-View Geometry in Computer Vision*], vol. 2 (01 2003).

[25] Zhang, Z., "A flexible new technique for camera calibration," *Pattern Analysis and Machine Intelligence, IEEE Transactions on* **22**, 1330 – 1334 (12 2000).

[26] Heikkilä, J. and Silvén, O., "A four step camera calibration procedure with implicit image correction," *Proceedings of the IEEE Computer Society Conference on Computer Vision and Pattern Recognition* **22**, 1106– (01 1997).

[27] Scaramuzza, D., Martinelli, A., and Siegwart, R., "A toolbox for easily calibrating omnidirectional cameras," *IEEE International Conference on Intelligent Robots and Systems* (10 2006).

[28] Brown, D., "Close-range camera calibration," *Photogramm. Eng.* **37** (12 2002).

[29] Muja, M. and Lowe, D., "Fast approximate nearest neighbors with automatic algorithm configuration.," *VISAPP 2009 - Proceedings of the 4th International Conference on Computer Vision Theory and Applications* **1**, 331–340 (01 2009).

[30] Elseberg, J., Magnenat, S., Siegwart, R., and Nuchter, A., "Comparison on nearest-neigbour-search strategies and implementations for efficient shape registration," *Journal of Software Engineering for Robotics (JOSER)* **3**, 2–12 (01 2012).

[31] Alex, R. and Alessandro, L., "Clustering by fast search and find of density peaks," *Science* **344**, 1492–1496 (01 2014).

[32] Hoppe, H., Derose, T., Duchamp, T., McDonald, J., and Stuetzle, W., "Surface reconstruction from unorganized points," *ACM SIGGRAPH Computer Graphics* **26**, 71–78 (07 1992).